

Fig. 3. Circuit diagram of the fully differential potentiostat.

mode interference rejection. In order to cover a wide dynamic range of input currents a current-to-frequency ADC is utilized. The proposed potentiostat provides over 70dB dynamic range of a differential current-mode input.

II. CHANNEL VLSI ARCHITECTURE

The top level architecture of the potentiostat is shown in Fig. 2. The input redox current is first converted to a voltage which is subsequently quantized by the ADC.

Amperometry and cyclic voltammetry detection techniques rely on the accuracy of the potential difference between the working and reference electrodes. The negative capacitive feedback around an operational transconductance amplifier (OTA) and the input common-mode feedback circuit set a fixed voltage at the two working electrodes, as detailed in the next section. An external voltage source drives the reference electrode to set the redox potential (shown connected to ground in Fig. 1 for simplicity).

The ADC utilizes the current-to-frequency quantization architecture. During the conversion period the redox current is integrated across a capacitor, C_{INT} . As soon as the capacitor voltage reaches a known value, V_{REF} , a reset pulse is generated by the comparator in order to discharge the integrating capacitor, as shown in Fig. 2. The input current is related to the number of pulses generated as

$$I_{IN} = \frac{NC_{INT}V_{REF}}{T_{conv}}, \quad (1)$$

where I_{IN} is the input current, T_{conv} is the conversion time, N is the number of comparator pulses, C_{INT} is the integrating capacitance, and V_{REF} is the comparator reference voltage.

III. VLSI CIRCUIT IMPLEMENTATION

An array of 96 integrated potentiostats was designed and implemented in a $0.35\mu\text{m}$ double-poly four-metal standard CMOS process. The redox current generated on on-chip working electrodes is accumulated on a capacitor and converted to the digital domain by a current-to-frequency ADC, as detailed in Fig. 3.

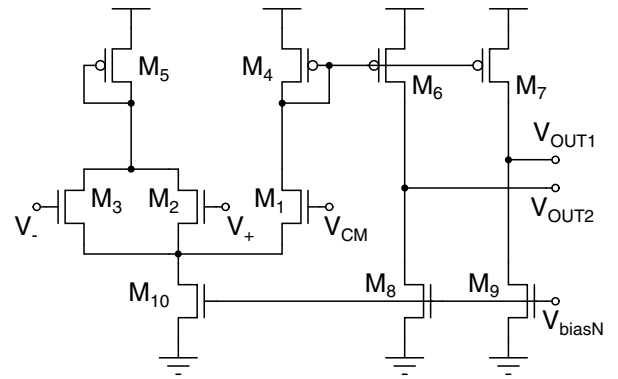


Fig. 4. Input common-mode feedback amplifier.

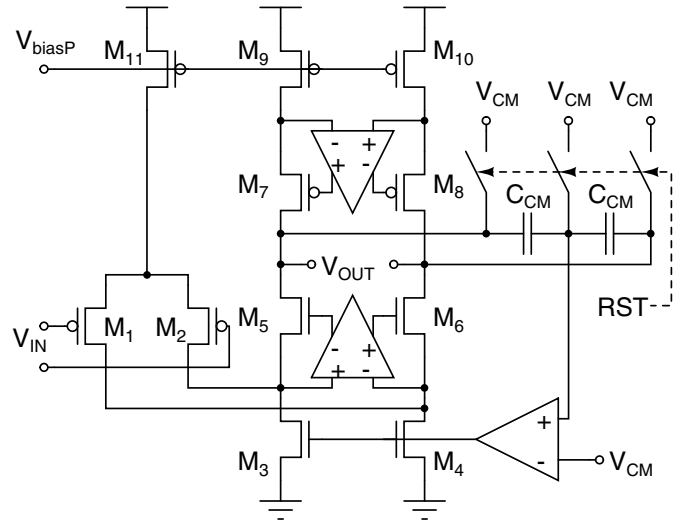


Fig. 5. Fully differential folded-cascode OTA along with the switched capacitor output CMFB circuit.

A. Current-to-Voltage Converter

A capacitive transimpedance amplifier (TIA) is employed to convert the input redox current to a voltage. The capacitive TIA has an averaging behavior and acts as a low-pass filter to remove the high-frequency noise. A common-mode regulation loop is necessary to prevent the high-impedance input node voltages from drifting to the positive or negative voltage levels. Fig. 3 shows an amplifier configured in a negative feedback to ensure a fixed input common-mode voltage. The amplifier circuit diagram is depicted in Fig. 4. The input differential pair transistors, $M_{2,3}$, sense the common-mode voltage. The common-mode voltage is compared with a desired value, V_{CM} , by transistors M_{1-3} in order to set the input common-mode voltage of the TIA.

Fig. 5 depicts the schematic of the fully differential OTA with the output common-mode feedback circuit. A simple switched capacitor circuit controls the output common-mode voltage. The RST signal is high once in a conversion period to refresh the voltage of the capacitors C_{CM} . The gain-enhanced folded-cascode topology improves the gain of the OTA and minimizes errors due to its finite gain. The closed-loop gain

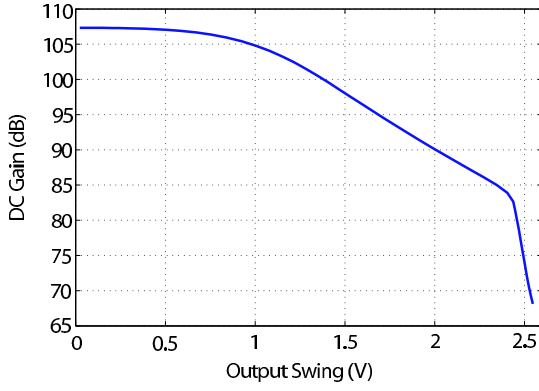


Fig. 6. Dependency of the OTA gain on the differential output swing.

TABLE I
OTA SIMULATED ELECTRICAL CHARACTERISTICS

DC gain	108dB
Unity Gain Frequency (0.5pF load)	20MHz
Slew Rate	13V/ μ s
Differential output Voltage Swing	$2V_{pp}$
Total Bias Current	16μ A
Supply Voltage	3.3V

error due to the finite gain of the OTA can be expressed as [?]

$$\Delta G = \left[1 - \frac{1}{1 + \frac{C_{IN}}{C_{INT}A}} \right] \times 100, \quad (2)$$

which for $\frac{C_{IN}}{C_{INT}A} \ll 1$ reduces to

$$\Delta G \approx \frac{C_{IN}}{C_{INT}A} \times 100, \quad (3)$$

where A is the finite gain of the OTA, C_{INT} is the integrating capacitance and C_{IN} is the sum of the capacitances at the input of the OTA. The simulated characteristics of the fully differential OTA are presented in Table I.

B. Analog-to-Digital Converter

The current-to-frequency conversion technique offers a wide dynamic range at the cost of low conversion rate. The ADC is comprised of a comparator and a counter. In order to achieve a fast response, a multi-stage comparator is employed in the ADC. A differential difference pair at the input of the first stage compares a differential input with a differential reference voltage. The second stage increases the overall gain of the comparator and the third stage acts as a level shifter to make the output voltage compatible with CMOS logic.

To save silicon area a compact linear feedback shift register (LFSR) is employed as a counter. During the conversion time it counts the number of pulses generated by the comparator and streams out the one-bit digital output at the end of each conversion time.

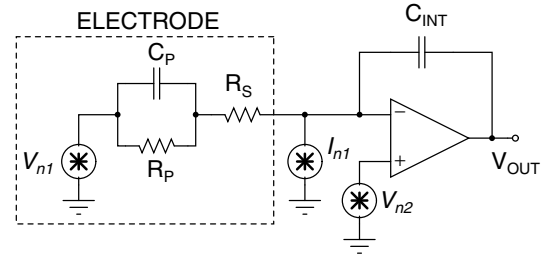


Fig. 7. Potentiostat front end with noise sources and an electrode equivalent model.

IV. NOISE ANALYSIS

In this section the noise performance of the proposed potentiostat is investigated. Fig. 7(a) shows a simplified circuit model of the potentiostat front end. The three noise sources in this circuit are: V_{n1} which represents the noise of the electrode, V_{n2} which accounts for the input-referred noise of the OTA, and I_{n1} that models the noise contribution of the input common-mode feedback amplifier. At low frequencies the series resistance of the electrode, R_S , is negligibly small, resulting the input-referred current noise equal to

$$\overline{I_{n,IN}^2} = \left| j\omega C_P + \frac{1}{R_P} \right|^2 (\overline{V_{n1}^2} + \overline{V_{n2}^2}) + \overline{I_{n1}^2}. \quad (4)$$

In order to minimize the input-referred noise and accordingly improve the sensitivity of the potentiostat, all the three terms in equation (4) should be minimized.

The first stage of the common-mode amplifier including input transistors M_{1-3} and the current mirror transistor M_4 , as well as the output stage including transistors M_{6-9} are the two noise sources in the common-mode feedback circuit. The noise of the first part appears as a common-mode signal at the input of the OTA which is removed due to its high common-mode rejection. As a result, the only sources of the noise are the output stage transistors M_{6-9} . This noise is composed of the thermal and flicker ($\frac{1}{f}$) noises as follows

$$\overline{I_n^2} = 4kT\gamma(g_{m7} + g_{m9}) + \frac{K}{C_{OX}f} \left(\frac{g_{m7}^2}{W_7L_7} + \frac{g_{m9}^2}{W_9L_9} \right), \quad (5)$$

where k is the Boltzmann constant, T is the absolute temperature, γ is a technology-dependent constant, g_m is the transconductance of the transistor, K is the $\frac{1}{f}$ noise constant, C_{OX} is the gate oxide capacitance, and W , L are the width and length of a transistor, respectively.

According to equation (5) for a fixed current, transistors operating in the strong inversion region have minimum noise contribution. The operation of transistors in the strong inversion region entails use of long transistors which also causes smaller γ and less $\frac{1}{f}$ noise [?]. The transistors utilized in the OTA and the input common-mode feedback amplifier are chosen based on the above calculations.

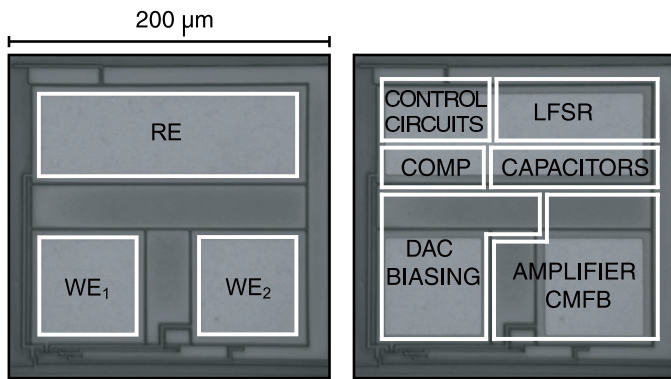


Fig. 8. Potentiostat die micrograph (depicted twice) showing the electrodes location (left) and the circuits floorplan (right). The channel size is $200\mu\text{m}\times 200\mu\text{m}$ in a $0.35\mu\text{m}$ CMOS process.

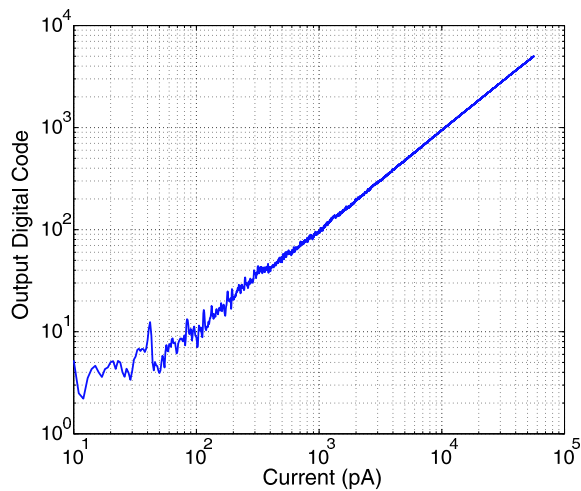


Fig. 9. Experimentally measured current transfer characteristic of the potentiostat.

V. EXPERIMENTAL RESULTS

Fig. 8 shows the die micrograph of the fully differential integrated potentiostat fabricated in a $0.35\mu\text{m}$ standard CMOS technology. The channel has differential on-chip working electrodes. In order to validate the functionality and utility of the potentiostats, electrical and chemical characterization experiments were performed. A testing PCB interfaces with a computer through FIFOs implemented on an FPGA. A low-level current was generated by applying the output of a voltage-mode digital-to-analog converter (DAC) across a large resistor. By sweeping the digital input of the DAC a ramp current is applied to the potentiostat. Fig. 9 shows the transfer characteristic of the integrated potentiostat.

In order to test the utility of the integrated potentiostat, a cyclic voltammetry experiment was also performed. Fig. 10 shows the experimentally recorded cyclic voltammogram of a phosphate buffered silane solution with a scan rate of $100\text{V}/\text{sec}$ recorded by one channel of the proposed potentiostat.

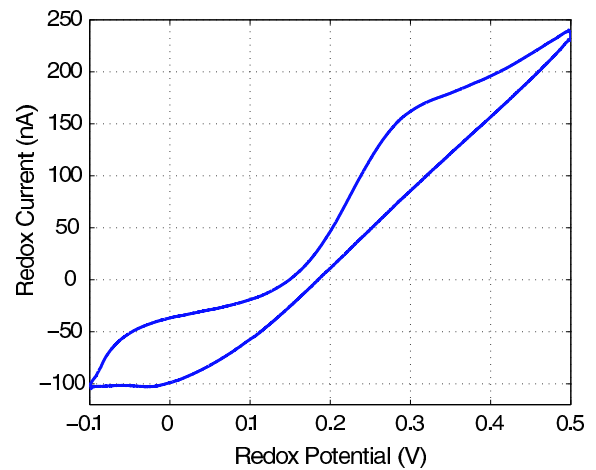


Fig. 10. Cyclic voltammogram performed with one channel on a phosphate buffered silane solution.

VI. CONCLUSIONS

A fully differential integrated potentiostat with differential recording electrodes for biochemical sensing in noisy environments is presented. Experimental results validate the utility of the potentiostat in wide dynamic range recording. In-channel analog-to-digital converter facilitates interfacing the microsystem with a digital signal processing unit and offers the parallelism in recording and data acquisition in a multi-channel setting.

REFERENCES

- [1] D.J. Michael and R.M. Wightman, "Electrochemical monitoring of biogenic amine neurotransmission in real time," *Journal of Pharmaceutical and Biomedical Analysis*, vol. **19**, pp. 33-46, 1999.
- [2] D.L. Robinson, B.J. Venton, M.L.A. Heien, and R.M. Wightman, "Detecting subsecond dopamine release with fast-scan cyclic voltammetry in vivo," *Clinical Chemistry*, vol. **49**, pp. 1763-1773, 2003.
- [3] R.J. Reay, S.P. Kounaves, and G.T.A. Kovacs, "An integrated CMOS potentiostat for miniaturized electroanalytical instrumentation," *IEEE Int. Solid-State Circuits Conference (ISSCC'94)*, pp. 162-163, 1994.
- [4] R. Genov, M. Stanacevic, M. Naware, G. Cauwenberghs, and N. Thakor, "16-channel Integrated potentiostat for distributed neurochemical sensing," *IEEE T. Circuits and Systems I*, vol. **53**, no. 11, pp. 2371-2376, November 2006.
- [5] M. Stanacevic, K. Murari, G. Cauwenberghs, and N. Thakor, "16-channel wide-range VLSI potentiostat array," *IEEE Trans. Biomedical Circuits and Systems*, 2004.
- [6] A. Bandyopadhyay, G. Mulliken, G. Cauwenberghs, and N. Thakor, "VLSI potentiostat array for distributed electrochemical neural recording," *IEEE Int. Circuits and Systems (ISCAS'02)*, vol. **2**, pp. 740-743, May 26-29, 2002.
- [7] A. Hassibi and T.H. Lee, "A Programmable electrochemical biosensor array in $0.18\mu\text{m}$ standard CMOS," *IEEE Int. Solid-State Circuits Conference*, vol. **1**, pp. 564-565, 2005.
- [8] M. Augustyniak, C. Paulus, R. Brederlow, N. Persike, G. Hartwich, D. Schmitt-Landsiedel, and R. Thewes, "A 24×16 CMOS-based chronocoulometric DNA Microarray," *IEEE Int. Solid-State Circuits Conference*, vol. **1**, pp. 59-68, 2006.
- [9] K. Murari, M. Stanacevic, G. Cauwenberghs, and N. Thakor, "Integrated Potentiostat for Neurotransmitter Sensing," *IEEE Engineering in medicine and biology magazine*, vol. **24**, 2005.
- [10] R.F.B. Turner, D.J. Harrison, and H.P. Baltes, "A CMOS potentiostat for amperometric chemical sensors," *IEEE Journal of Solid-State Circuits*, vol. **22**, 1987.